METRICA
METRology Institutional CAtalog

ISTITUTO NAZIONALE DI RICERCA METROLOGICA
Repository Istituzionale

Droplet orthogonal impact on nonuniform wettability surfaces

(Article begins on next page)

31 January 2025

Droplet WILEY

Droplet orthogonal impact on nonuniform wettability surfaces

Shashwata Moitra[1] | Mohamed Elsharkawy[1] | Antonio Russo[2] | Sreya Sarkar[1] |
Ranjan Ganguly[3] | Pietro Asinari[2] | Constantine M. Megaridis[1]

[1]Department of Mechanical and Industrial Engineering, University of Illinois Chicago, Chicago, Illinois, USA

[2]Energy Department, Politecnico di Torino, Torino, Italy

[3]Department of Power Engineering, Jadavpur University, Kolkata, West Bengal, India

Correspondence
Constantine M. Megaridis, Department of Mechanical and Industrial Engineering, University of Illinois Chicago, Chicago, IL 60607-7022, USA.
Email: cmm@uic.edu

Abstract

The vast majority of prior studies on droplet impact have focused on collisions of liquid droplets with spatially homogeneous (i.e., uniform-wettability) surfaces. But in recent years, there has been growing interest on droplet impact on nonuniform wettability surfaces, which are more relevant in practice. This paper presents first an experimental study of axisymmetric droplet impact on wettability-patterned surfaces. The experiments feature millimeter-sized water droplets impacting centrally with $We < 100$ on a flat surface that has a circular region of wettability θ_1 (Area 1) surrounded by a region of wettability θ_2 (Area 2), where $\theta_1 < \theta_2$ (i.e., outer domain is less wettable than the inner one). Depending upon the droplet momentum at impact, the experiments reveal the existence of three possible regimes of axisymmetric spreading, namely (I) interior (only within Area 1) spreading, (II) contact-line entrapment at the periphery of Area 1, and (III) exterior (extending into Area 2) spreading. We present an analysis based on energetic principles for $\theta_1 < \theta_2$, and further extend it for cases where $\theta_1 > \theta_2$ (i.e., the outer domain is more wettable than the inner one). The experimental observations are consistent with the scaling and predictions of the analytical model, thus outlining a strategy for predicting droplet impact behavior for more complex wettability patterns.

INTRODUCTION

Droplet impact on flat surfaces is a long-studied problem dating back to Worthington's pioneering studies conducted 150 years ago.[1] Since then, research on droplet impact has proliferated.[2–4] Many theoretical and experimental studies have been performed to analyze, evaluate, and predict the behavior of impacting droplets.[5] Prior reports have ranged from studying fundamental parameters affecting spreading,[6–8] receding[9,10] and total[11–14] or partial rebound[14] of droplets impacting on surfaces of known fixed wettability, to altering the total contact time[15,16] between droplet and surface. As significant and influential as all these studies have been, their vast majority studied uniform-wettability surfaces.[17,18] In contrast,

common-day surfaces mostly exhibit spatially nonuniform wettability. Certain industrial and engineering technologies where these nonuniform wettability surfaces are used, include enhanced phase-change heat transfer,[19–22] inkjet printing on heterogeneous surfaces, or solder droplet deposition on electronic circuits, which are inherently nonuniform. Furthermore, droplet impact on engineered surfaces is seen in emerging areas, such as droplet-based electricity generators,[23] efficient direct cooling at ultra-high solid temperature,[24] and so on. Whether by fabrication, design, or nature, most surfaces contain structural or chemical imperfections and heterogeneity that engender spatial domains of varying wettability on them.

There has been a growing interest and recent studies on surfaces with wettability contrast. Wettability-patterned surfaces, as they are

sometimes called in the literature,[25] are engineered surfaces that deploy specifically designed spatial distributions of high- and low-surface energy domains on a single substrate. Such surfaces have been studied in recent times to demonstrate their potential in various areas that include high-rate fluid transport,[25] enhanced condensation,[21] droplet manipulation,[26,27] water capture from the atmosphere and water harvesting,[28–30] selective droplet sliding,[31] area-selective cooling,[32] passive and active liquid transport,[33,34] enhanced heat transfer,[35–37] and so on. Although wettability patterning is now utilized for a multitude of applications, our focus here lies on the droplet impact phenomenon on spatially nonuniform wettability surfaces. There exist some numerical studies[38–41] in the literature on droplet impact on nonuniform wettability targets, but far fewer experimental studies in this area have attempted to combine theoretical models with experimental observations.[42,43] Kim et al.[44] studied the behavior of droplets striking a superhydrophobic surface with hydrophilic annuli and demonstrated the ability to utilize these patterned-wettability surfaces to achieve varying liquid deposit morphologies. Mock et al.[45] studied droplet impact on hydrophobic polymer surfaces that were patterned lithographically to yield circular hydrophilic domains. They observed a spontaneous self-centering effect that droplets exhibited when striking the aforementioned surfaces. Michel et al.[46] presented a theoretical model to elucidate the hydrodynamics of impacting droplets on the surfaces described in Mock et al.[45] Schutzius et al.[47] studied an interesting phenomenon of vectoring and shaping of impacting droplets on wettability-patterned surfaces; a follow-up numerical simulation of the phenomenon was reported by Zhang et al.[48] Vaikuntanathan et al.[42] presented an experimental study of the water-droplet impact on the contrast line between the hydrophilic and the hydrophobic domains of a dual-textured surface. They developed a quantitative analysis of the spreading and retraction of the droplet post-impact. Vaikuntanathan et al.[43] studied the bulk movement of water droplets impacting the contrast line between a smooth and a textured surface and also developed a model, that was validated against the experimental results. They observed that the impacting drop had a net horizontal velocity toward the more wettable area, while the net displacement decreased with increasing Weber number. Sprittles and Shikhmurzaev[49] and Russo et al.[50] numerically simulated droplet impact on wettability-patterned surfaces where different impact behaviors for example, droplet translation, splitting, and vectoring were described. Farshchian et al.[51] demonstrated control of rebound trajectories on wettability-patterned surfaces by changing the degree of contrast; a numerical simulation study of a similar phenomenon was reported by Yuan et al.[39] For directional rebounding of the water droplets, they found that the post-rebound landing distance increased with increasing Weber number and higher wettability contrasts. Xu et al.[52] studied how the size of hydrophilic circular regions surrounded by superhydrophobic back-grounds can affect the pinch-off dynamics of impacting droplets. They reported partial rebound of the droplet impacting on their wettability-patterned surfaces even at moderate or large Weber numbers. They also studied single-drop and multidrop pinch-off, which depended on wall adhesion and the nature of capillary waves formed due to the kinetic energy of the droplets. Sen et al.[53] studied drop impact on a step wettability-patterned metal mesh and characterized post-impact behavior depending upon the impact velocity. They showed that the droplet half on the superhydrophilic domain got pinned, while the other droplet half on the superhydrophobic domain rebounded obliquely and exhibited a vectoring tail that detached only when the vectoring velocity was too high. Satpathi et al.[54] experimented on patterned surfaces where they impacted a droplet on a superhydrophilic spot surrounded by a superhydrophobic region. They studied the different regimes that the droplet exhibited depending on the spot size and the impact Weber number and also modeled the maximum spreading extent. However, their model neglected the energy required to crossover from a more wettable to a less wettable region. That study also did not consider the different regimes of spreading due to the cross-over energy barrier and the liquid entrapment at the wettability contrast line. While the above-mentioned studies addressed various aspects and the potential of wettability-patterned surfaces, a consolidated study of maximum droplet spreading and how it is affected by spatially nonuniform wettability is lacking.

We aim to add to the literature by studying analytically the dynamics of droplets spreading on a nonuniform wettability surface, and by characterizing experimentally the axisymmetric droplet impact on a circular region (with specific wettability) surrounded by a region of different wettability. While this arrangement is admittedly simple, it provides a first step toward more complex configurations with random wettability patterns—a problem that can be addressed more accurately with detailed 3D models. In this work, we employ a simple model that can predict droplet spreading behavior depending on the impact Weber number and the wettabilities of the two regions (as characterized by the respective advancing contact angles). The work draws upon the previously reported models of Pasandideh-Fard et al.,[55] Mao et al.,[56] and Ukiwe and Kwok[57] to provide a renewed analytical understanding of droplet axisymmetric impact on non-uniform wettability surfaces. From experiments and theory for cases where the inner domain is more wettable than the surrounding one, we discuss the existence of a cross-over energy barrier at the transition line between the two regions of wettability, leading to three possible spreading regimes. We also extend the model to demonstrate its utility to predict the spreading regimes when the outer domain is more wettable than the inner one. Last, the analytical model provides guidance for predicting the maximum lateral fluid spread in more complex cases where the front of a droplet encounters a wettability step line on the underlying substrate.

RESULTS AND DISCUSSION

In the classical configuration, a droplet of diameter D_o strikes a uniform-wettability smooth surface with velocity U_o. The dynamic phenomena and impact outcome are determined by the Weber number $We = \rho U_o^2 D_o / \sigma$, where ρ, σ are, respectively, the density and surface tension of the fluid. The inertial forces from the impact cause the formation of a liquid rim, which continues to advance and spread
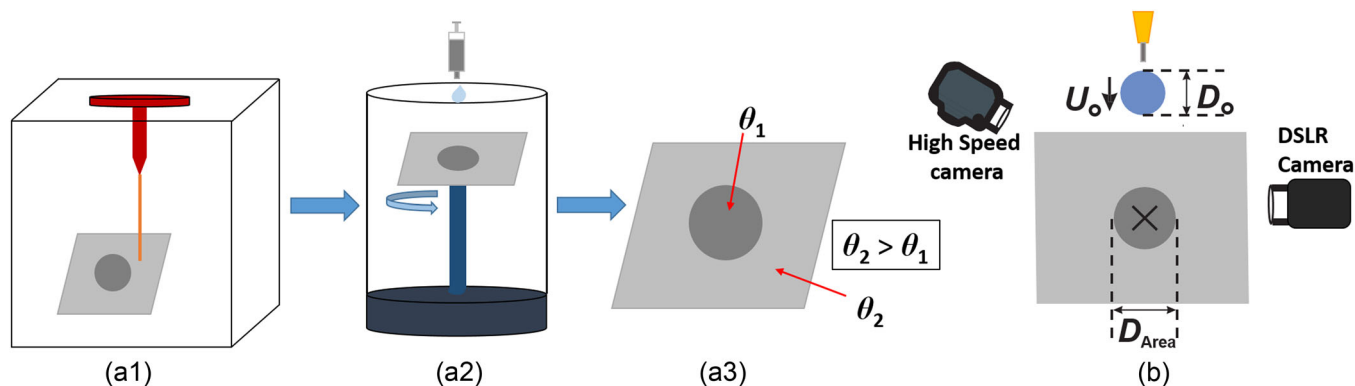
FIGURE 1 Schematic of the wettability-patterned sample preparation steps and experimental setup. (a1) Laser etching of the aluminum sample to impart surface roughness. (a2) Spin-coating of a thin Teflon film on the laser-processed samples. (a3) The result is a surface possessing two distinct domains of wettability: θ_1 = 124° (advancing contact angle on Teflon-coated smooth aluminum), and θ_2 = 157° (advancing contact angle on Teflon-coated laser-processed aluminum). (b) Schematic of the experimental setup for visualizing droplets of diameter $D_\circ$ impacting at the center of a circular domain (diameter D_{Area}, wettability θ_1) with velocity $U_\circ$. Visualization was performed with a dual-camera setup to ensure that the droplets impacted centrally and that the subsequent events remained axisymmetric.

laterally on the surface. While advancing, the rim forms an angle θ with the surface; this angle is the advancing contact angle. The rim eventually attains a maximal spreading diameter D_{Max}. The maximal spreading factor, defined by $\eta_{\text{Max}} = D_{\text{Max}}/D_\circ$, has been the object of many prior studies on the spreading behavior of impacting droplets.[57] Multiple studies have shown a strong correlation between theoretical predictions and independent experimental results. These reports demonstrated the spreading behavior to be a complex interplay between inertial, capillary, and viscous forces, with a strong dependence on the underlying wettability of the target surface.[10]

In the present system (Figure 1), the water droplets impact at the center of disks of diameter D_{Area} (advancing contact angle θ_1) surrounded by a region of advancing contact angle θ_2, where $\theta_2 > \theta_1$. The sample preparation technique of the wettability-patterned surfaces is shown in Figure 1a1–a3 (see Methods section for details). Under these conditions, three outcomes are possible depending on the value of We (Figure 2). For the lower range of We (Figure 2a), the spreading of the impacting droplet occurs entirely within the inner disk region. The second outcome occurs for a medium range of We, where the droplet spreads, encounters the boundary between the two wettability regions, and does not possess enough energy to spread beyond the inner region, resulting in $D_{\text{Max}} = D_{\text{Area}}$ and $\eta_{\text{Max}} = \eta_{\text{Area}}$ (Figure 2b). The third outcome occurs at higher values of We, where the droplet possesses enough energy to spread beyond the disk periphery (Figure 2c). Henceforth, we will denote these three regimes as (1) Regime I—interior spreading, (2) Regime II—entrapment at the wettability contrast line, and (3) Regime III—exterior spreading. In the following section, we derive analytically and show experimentally the range of We where each of these regimes is observed.

In the low Weber number regime, that is, Regime I (interior spreading), the impacting droplet does not possess enough energy to reach—at its maximum spread—the wettability contrast line (WCL), where the wettability change occurs (Figure 2a). The maximum spreading can be predicted using existing energy approach models of droplet impact on uniform-wettability surfaces. For the sake of

completeness, we briefly repeat this derivation. Considering a droplet with diameter $D_\circ$ and velocity $U_\circ$, the kinetic and surface energies are expressed as $E_{K1} = \frac{1}{2}\rho\frac{\pi D_\circ^3}{6}U_\circ^2$, $E_{S1} = \pi D_\circ^2\sigma$.[55,58–60] Upon impact, the droplet spreads, and the liquid momentarily ceases upon reaching its maximum lateral spread. Assuming the kinetic energy of the droplet to be zero at its maximum spread, the total energy of the system before contact and at maximum spread can be expressed as

$$E_{S1} + E_{K1} = E_{S2} + E_{\text{wet-dry}} + W_{\text{losses}}, \quad (1)$$

where E_{S2} is the surface energy of the droplet (of the liquid–gas interface) at its maximum spread, W_{losses} are the viscous losses sustained during spreading, and $E_{\text{wet-dry}}$ is the energy due to the wetting of the solid surface. The above energy representation has been reported multiple times, with one of the most accurate depictions put forth by Ukiwe and Kwok.[57] Following certain mathematical and geometric assumptions, the above terms can be expressed[a] as $E_{S2} = \sigma\left(\frac{\pi}{4}D_{\text{Max}}^2 + \frac{2}{3}\pi\frac{D_\circ^3}{D_{\text{Max}}}\right)$, $E_{\text{wet-dry}} = -\sigma\frac{\pi}{4}D_{\text{Max}}^2\cos\theta_1$, and $W_{\text{losses}} = \frac{\pi}{3}\rho U_\circ^2 D_\circ D_{\text{Max}}^2\frac{1}{\sqrt{Re}}$, where Re is the Reynolds number $Re = U_\circ D_\circ/v$ and v is the dynamic viscosity of the fluid. Substituting the above terms, Equation (1) can be expressed in terms of the salient parameters as

$$(We + 12)\eta_{\text{Max}} = 8 + \eta_{\text{Max}}^3\left[3(1 - \cos\theta_1) + 4\frac{We}{\sqrt{Re}}\right], \quad (2)$$

as originally reported by Ukiwe and Kwok.[57] If the impact conditions (We, Re) and wettability (advancing contact angle θ_1) of the surface are known, then the maximum spreading factor (η_{Max}) for droplets spreading entirely within the innermost region can be evaluated readily using Equation (2).

In Regime II, liquid entrapment at the wettability step occurs when the total energy of the impacting droplet is high enough for the

---

[a]For detailed derivations, see Pasandideh-Fard et al.,[55] Mao et al.,[56] and Ukiwe and Kwok.[57]
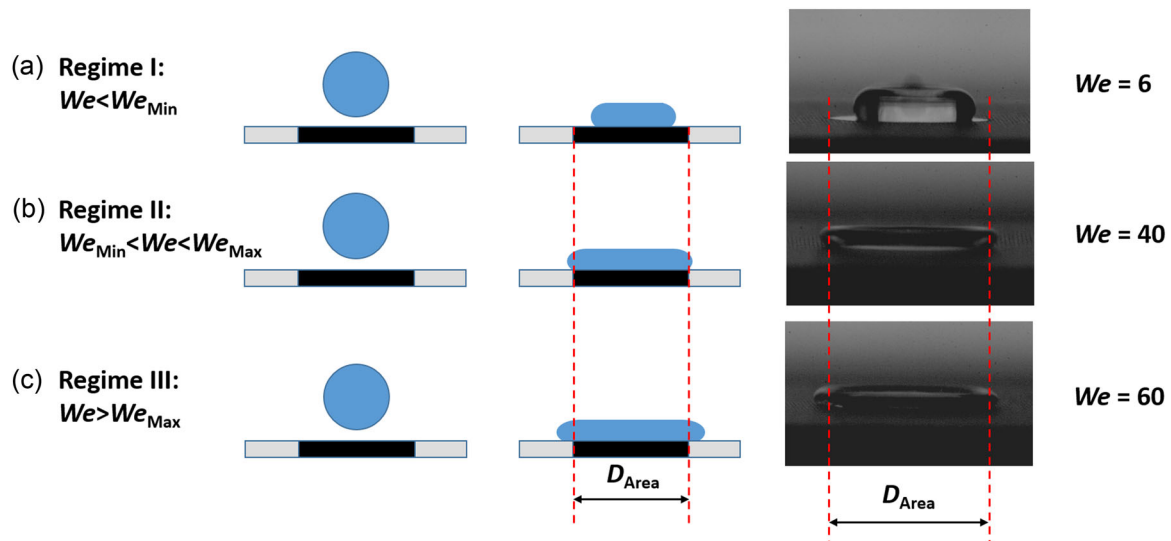
FIGURE 2 When water droplets of a certain diameter D_o impact centrally a circular domain (diameter D_{Area}), three possible outcome regimes exist depending on the impact velocity U_o (which designates the corresponding value of We). (a) Regime I (interior spreading)—droplet spreading occurs entirely within the circular domain, thus $D_{Max} < D_{Area}$. (b) Regime II (contact line entrapment)—the droplet reaches the periphery of the inner domain and gets pinned at the wettability contrast line (WCL), thus $D_{Max} = D_{Area}$. As the impact velocity increases further, the liquid remains anchored at the WCL until the energy is high enough to extend beyond the WCL. (c) Regime III (exterior spreading)—the droplet impacts and spreads past the WCL, thus $D_{Max} > D_{Area}$. The three regimes occur over specific ranges of We. The images at right show droplets of $D_o = 2.1$ mm at their maximal lateral spread at three different We, each corresponding to one of the three impact regimes.

fluid rim to reach the WCL but not as high to overcome the cross-over energy required to surpass this energetic barrier (Figure 3). As long as the impact velocity (likewise We) is below a threshold value, an impacting droplet remains trapped within the innermost region. Beyond the threshold impact velocity, the droplet can cross the WCL barrier and continue its spreading onto the exterior region (contact angle θ_2), thereby giving rise to Regime III.

The minimum Weber number, We_{Min}, at which the droplet covers the entire Area 1 can be determined from Equation (2). Since D_{Area} is known, we retroactively solve for We_{Min}. Thus, with $D_{Max} = D_{Area}$, it is $\eta_{Max} = \eta_{Area}$, and We_{Min} can be derived from Equation (2) which takes the form

$$(We_{Min} + 12)\eta_{Area} = 8 + \eta_{Area}^3 \left[3(1 - \cos\theta_1) + \frac{4We_{Min}}{\sqrt{Re}} \right]. \quad (3)$$

As impact velocity (likewise We) rises further, impacting droplets remain entrapped at the WCL, but fail to extend into the exterior region 2. This behavior persists until We exceeds a critical value, We_{Max}, when the liquid front overcomes the energetic barrier and spreads onto the exterior surface. To help understand entrapment, we consider a static droplet sitting on a surface of uniform wettability, θ. The total liquid surface energy, E_σ, can be expressed as

$$E_\sigma = \sigma A_t - w_a A_{ls}, \quad (4)$$

where A_t is the total surface area of the liquid–gas interface, w_a is the work of adhesion $w_a = \sigma(1 + \cos\theta)$, and A_{ls} the liquid–solid contact area. We now consider the pinned droplet in a static sense and analyze

two instances in time, just when the rim reaches the WCL (Figure 3b-i), and right before it surpasses it (Figure 3b-ii). The surface free energy of both of these configurations can be expressed as follows, $E_{\sigma,1} = \sigma A_{t,1} - \sigma(1 + \cos\theta_1)A_{ls,1}$ and $E_{\sigma,2} = \sigma A_{t,2} - \sigma(1 + \cos\theta_2)A_{ls,2}$. Since the outer rim of the liquid droplet during that period remains fixed on the WCL, then $A_{ls,1} = A_{ls,2} = A_{ls} = \pi D_{Area}^2/4$. Since A_{ls} is fixed and the volume of a single droplet is very small ~ 4.7 µL, as the droplet spreads out in the form of a thin pancake, the height change from state 1 to 2 is negligible, and thus we can assume that $A_{t,1} = A_{t,2}$ (see Supporting Information for details). The energy difference $E_{\sigma,2} - E_{\sigma,1}$ between these two states (Figure 3c) can then be expressed as

$$\Delta E_{bar} = E_2 - E_1 \cong E_{\sigma,2} - E_{\sigma,1}$$
$$\cong \frac{\sigma \pi D_{Area}^2}{4}(\cos\theta_1 - \cos\theta_2). \quad (5)$$

This ΔE_{bar} is the cross-over energy barrier that must be overcome by the spreading droplet in order for the liquid to traverse beyond the WCL. The existence of this cross-over energy can also be explained in terms of the need of the droplet to adjust its contact angle to continue its advancement onto the exterior region. We have observed the change in contact angle experimentally. From Equation (5), whenever θ_2 is greater than θ_1 (i.e., region 1 is relatively more wettable than region 2), ΔE_{bar} is positive, meaning that the liquid must transition from a lower energy state to a higher one, and thus, if this energy differential is not available, the expanding droplet can not spread onto the exterior region. To determine We_{Max}, the value of We where an impacting droplet
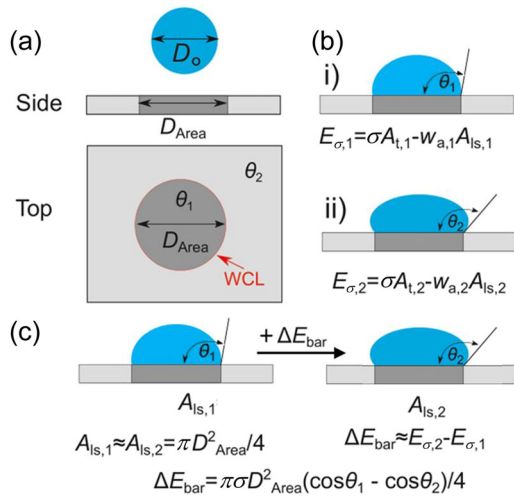
FIGURE 3 Schematic depiction of droplet impact transition from Regime II to Regime III. (a) A droplet of diameter D_o strikes orthogonally the center of a circular region of wettability θ_1 (advancing contact angle) and diameter D_{Area}. This area is surrounded by an infinite region of wettability θ_2 (advancing contact angle). The border between these two regions is referred to herein as the wettability contrast line (WCL). For the impacting droplet to spread beyond D_{Area}, the liquid must be able to change its contact angle from that of the inner region (b-i) to that of the outer region (b-ii). (c) During this change of the liquid–gas interface, the liquid/solid contact area (A_{ls}) remains the same. The additional energy required for this transition is denoted by ΔE_{bar}.

possesses sufficient energy to escape entrapment, we must first analyze Regime III—exterior spreading.

It is important to note in this context that the laser etching and Teflon coating technique, as described in the Methods section, creates a physical step from the etched (lowered) to the smooth domain on the substrate. Thus, there exists a vertical energy barrier (positive, if the inner region is Teflon-coated laser-etched Al, and negative otherwise) that has to be overcome in order for the droplet to continue its spreading beyond the WCL. The step size, measured using a KLA-Tencor P7 Stylus Contact Profilometer, was found to be 4.07 ± 0.42 μm (see Supporting Information for details). An order of magnitude analysis using Equation (5) derives $\Delta E_{bar} \sim O(10^{-6})$ J, while the vertical energy barrier[b] is $O(10^{-9})$ J. This implies that the vertical energy barrier at the WCL can safely be neglected for the present analysis.

Based upon the aforementioned analysis, we expect that for $We > We_{Max}$, an impacting droplet will enter Regime III, that is, exterior spreading. The analysis for Regime I clearly indicated that the maximum spreading diameter depends on the wettability of the underlying substrate. We next investigate the dependence of maximum spreading diameter in Regime III on the contact angles of both the underlying regions, which are in contact with the fluid. To

predict the maximum spreading in Regime III, we modify Equation (1) to account for nonuniform underlying wettability by altering only $E_{wet\text{-}dry}$ in the energy equation. The initial surface and kinetic energy terms remain the same due to the initial conditions being the same. The final surface energy and viscous losses are not altered due to the fact that they are originally derived with consideration only of the geometric shape and no dependence on the wettability. Thus, to evaluate how the nonuniform wettability of the underlying surface alters the maximum spreading diameter, one only needs to consider the energy needed for the liquid to wet the multiple wettability regions. In addition, we must take into consideration the role of the cross-over energy, ΔE_{bar}, which must be overcome for the fluid to reach out into Area 2. The cross-over energy, as already explained, arises from the need for the liquid–gas interface to change from one shape to another with a pinned contact line. This implies that ΔE_{bar} is of retarding nature, and must be accounted for in the energy equation. Thus, modifying Equation (1) to account for a droplet impacting a dual-wettability region, we obtain

$$E_{S1} + E_{K1} = E_{S2} + E_{wet\text{-}dry\text{-}1} + E_{wet\text{-}dry\text{-}2} \\ + W_{losses} + \Delta E_{bar}. \tag{6}$$

The above equation has the same form as Equation (1), but also takes into consideration the cross-over energy barrier (ΔE_{bar}) and that the droplet extends over two regions of distinct wettabilities. Substituting $E_{wet\text{-}dry\text{-}1} = -\sigma\frac{\pi}{4}D_{Area}^2\cos\theta_1$, and $E_{wet\text{-}dry\text{-}2} = -\sigma\frac{\pi}{4}(D_{Max}^2 - D_{Area}^2)\cos\theta_2$ in Equation (6), we deduce

$$E_{S1} + E_{K1} = E_{S2} - \sigma\frac{\pi}{4}D_{Max}^2\cos\theta_2 + W_{losses}, \tag{7}$$

which is Equation (1) for a droplet impacting a uniform-wettability surface (θ_2). η_{Max} can be determined using Equation (2) for θ_2. Yet, this solution holds only if We exceeds We_{Max}. To determine at what point impacting droplet transitions from the entrapment regime to the exterior spreading regime, we carry out the same procedure as in the previous section. Knowing that the transition from Regime II to Regime III occurs when $\eta_{Max} = \eta_{Area}$, we use the solution of Equation (7), retroactively solving the following equation for We_{Max}

$$(We_{Max} + 12)\eta_{Area} = 8 + \eta_{Area}^3\left[3(1 - \cos\theta_2) + \frac{4We_{Max}}{\sqrt{Re}}\right]. \tag{8}$$

Based on the above equations, it stands that the spreading of a droplet impacting a dual-wettability surface is unaffected by the wettability of the innermost region (θ_1). In other words, the spreading on the outermost region (θ_2) is independent of the wettability of the inner region. The only effect that the wettability of the innermost region has is in dictating at what We, the impacting droplet is able to transition from the entrapment regime to the exterior spreading regime. An impacting droplet can not reach the exterior region unless it possesses enough excess energy to change its liquid–gas interface until it attains the advancing angle characteristic of the exterior region. All excess energy is redistributed in this surface-area change. Once the transition has occurred, the maximum spreading diameter

[b]Difference in z-elevation between inner and outer region. This physical step alters the potential energy on each side of the WCL.

on the outer wettability region would be independent of the inner region. Or, the same maximum diameter would be achieved as if the droplet impacted on a surface of uniform wettability θ_2. Simply, Equation (2) solved either for We_{Max} or We_{Min} designates the dynamic domain over which entrapment occurs (We_{Min} to We_{Max}). We note that this conclusion is based on assumptions that the analysis relies on, and is supported by the experimental data presented in the next section.

The above analysis can be summarized in terms of how maximum spreading varies with We, as follows

$$\eta_{Max} = \begin{cases} \eta_I & We < We_{Min}, \\ \eta_{II} & We_{Min} < We < We_{Max}, \\ \eta_{III} & We > We_{Max}, \end{cases} \quad (9)$$

where η_I is the spreading factor in Regime I (interior spreading), as determined from $(We + 12)\eta_I = 8 + \eta_I^3\left[3(1 - \cos\theta_1) + 4\frac{We}{\sqrt{Re}}\right]$. η_{II} is the spreading factor in Regime II (entrapment on WCL), which is designated by the size of the inner disk, that is, $\eta_{II} = D_{Area}/D_o$. η_{III} is the spreading factor in Regime III (exterior spreading), as determined from $(We + 12)\eta_{III} = 8 + \eta_{III}^3\left[3(1 - \cos\theta_2) + 4\frac{We}{\sqrt{Re}}\right]$. We_{Min} and We_{Max} are the limits separating the three regimes; the respective values can be obtained from $(We_{Min} + 12)\eta_{Area} = 8 + \eta_{Area}^3\left[3(1 - \cos\theta_1) + \frac{4We_{Min}}{\sqrt{Re}}\right]$ and $(We_{Max} + 12)\eta_{Area} = 8 + \eta_{Area}^3\left[3(1 - \cos\theta_2) + \frac{4We_{Max}}{\sqrt{Re}}\right]$. The We range for entrapment (ΔWe_{trap}) in Regime II, extends from We_{Min} to We_{Max}.

We have verified the theoretical formulation by studying experimentally deionized (DI) water droplets of $D_o = 2.1$ mm impacting with varying velocities (likewise We) on samples with inner wettability $\theta_1 = 124°$ and outer wettability $\theta_2 = 157°$; see Figure 1b. Figure 4a,b demonstrates the salient behaviors predicted by the analysis. For low values of We, the droplet spreads and arrests before reaching the WCL. At a specific higher value of We, the droplet becomes entrapped at the WCL and fails to change its spreading factor (outer fluid rim remains pinned at the WCL). Then, at a specific higher value of We, the droplet is able to overcome the pinning at the WCL and continues its spreading over the less wettable outer region. We begin with a circle of $D_{Area} \approx 4$ mm, corresponding to $\eta_{Area} \approx 1.9$. Figure 4a plots the spreading of droplets with varying Weber numbers. The scaling and the theoretical predictions from the analytical formulation are consistent with the experimental trend. The deviation between analysis and experiments can be attributed to the dissipation of the kinetic energy at the outer rim of the expanding fluid which, albeit small in comparison to the rest of the energy terms in the equations, is not accounted for in the analytical formulation. Figure 4a demarcates the three domains of spreading. As inferred from the experimental image sequences, interior spreading is observed for low We, until the first sign of entrapment is observed at $We \approx 34$ for which the observed spreading of the droplet base corresponds to $\eta_{Max} = \eta_{Area}$; entrapment continues for rising We until the first sign of exterior spreading is observed at $We \approx 39$. For the case with $D_{Area} \approx 4.5$ mm (corresponding to $\eta_{Area} \approx 2.1$), the same trend is observed (Figure 4b). However, the entrapment in this case starts at $We \approx 38$, while exterior

spreading starts at $We \approx 45$. The range of We over which entrapment occurs is larger in the case of the larger disk.

After solving for We_{Max} and We_{Min} from Equations (3) and (8) for each experimental sample, one can determine ΔWe_{trap}, the range of We where $\eta_{Max} = \eta_{Area}$ and compare it with the experimental ΔWe_{trap}. For $\eta_{Area} = 1.9$ (Figure 4a), we obtain both the experimental and theoretical $\Delta We_{trap} \approx 5$. Similarly, for $\eta_{Area} = 2.1$, we calculate $\Delta We_{trap} \approx 7$ from the theoretical predictions, which is the same as the experimentally observed value (Figure 4b). As seen from these results, there is a strong agreement between the analytically predicted values and those observed experimentally for the range of We where the liquid transitions from barely reaching the wettability contrast line to when the liquid starts spreading beyond the disk. The We range (ΔWe_{trap}) over which the droplet becomes entrapped increases for larger D_{Area} (compare Figure 4a and 4b). But as observed from Figure 4a,b, although the theoretical and experimental trends are qualitatively similar and the range of ΔWe_{trap} is the same, the respective values of η_{Max} do not coincide due to the fact that the model predictions approximate the spreading losses and kinetic energy dissipation at the WCL. The energy dissipation at the WCL and the viscous spreading losses experienced by the spreading droplets could not be calculated precisely from this simple model. As a result, the η_{Max} predictions from the model are higher than the experimentally observed values, and thus the range of theoretical ΔWe_{trap} shifts to lower We values. While this simple analytical model could not predict the exact droplet spreading diameter, it captures the key characteristics of the various spreading regimes as well as the dynamics of droplet spreading and wetting.

It is apparent from Equation (7) and the related discussion that the spreading behavior in Regime III is insensitive to the wettability of the inner region and its area extent. This was corroborated by the experimental observations. We found no variation in the maximum spreading diameter (D_{Max}) in Regime III, regardless of the size of the inner domain. While this behavior is hinted at in Figure 4a,b, we verified this by impacting droplets with constant $We = 95$ on surfaces with hydrophobic, circular spots of different diameters, D_{Area} in less-wettable (superhydrophobic) surroundings. As seen in Figure 4c, at lower values of D_{Area} (≤5.5 mm), the observed D_{Max} does not change. In these cases, the small wettable domain cannot restrict the liquid, which extends beyond the WCL and eventually reaches a maximum spreading diameter $D_{Max} > D_{Area}$, before the droplet starts receding. For larger D_{Area} (>5.5 mm), the droplet becomes entrapped (Regime II), and $D_{Max} = D_{Area}$. Beyond $D_{Area} \sim 6.5$ mm, the spreading happens entirely within the inner region and thus, the maximum spreading diameter ($D_{Max} < D_{Area}$) varies with We.

In all cases considered so far, we considered that $\theta_1 < \theta_2$. We now explore situations where the reverse is true, that is, $\theta_1 > \theta_2$ implying that the outer region is relatively more wettable than the inner region. We begin by physically interpreting such circumstances, where a spreading droplet is impacting centrally on a circular domain that is less wettable than the outer area. Intuitively, and based upon the prior energy analysis, the impacting droplet would never experience an entrapment regime. If the droplet were to spread into
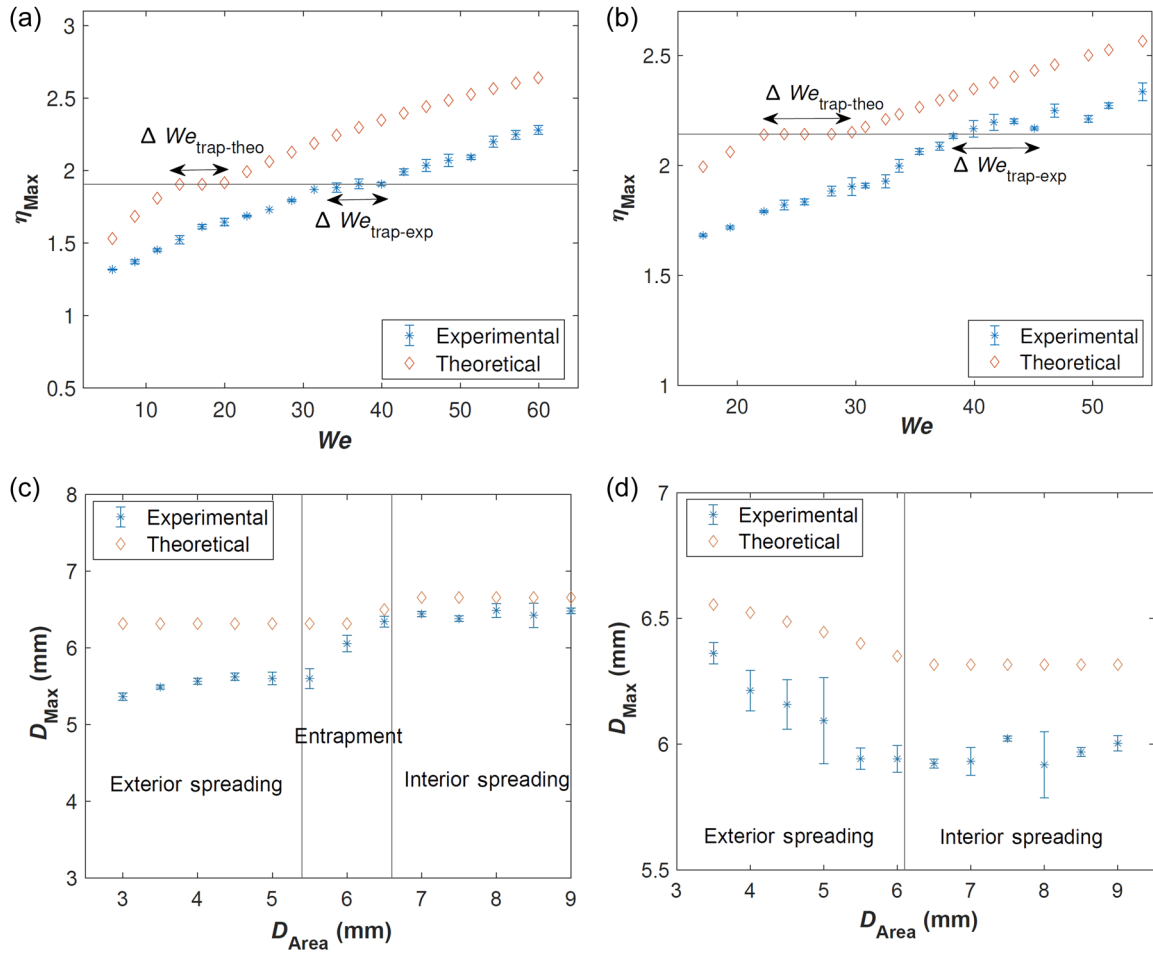
FIGURE 4 Maximum droplet spreading parameters for varying *We* and circular domain size. Droplet impact with varying *We* on circular domains with $\theta_1 = 124°$, droplet diameter $D_\circ = 2.1$ mm, and diameter D_{Area} equal to either (a) 4 mm, or (b) 4.5 mm. The surrounding domain (Area 2) has $\theta_2 = 157°$. In both cases, the maximum spreading factor increases as *We* rises. At a certain value (We_{Min}), the droplets become trapped at the disk periphery. After *We* reaches We_{Max}, the droplet overcomes entrapment and spreads onto the exterior less-wettable region. (c) At constant $We = 95$, $\theta_1 = 124°$, and $\theta_2 = 157°$, as the inner region diameter is increased progressively, the maximum spreading factor stays unchanged until the instant where the droplet becomes entrapped at the wettability contrast line (WCL) ($D_{Area} \approx D_{Max}$). Beyond a larger D_{Area} (≈6.5 mm), interior spreading is observed as the spreading D_{Max} remains relatively constant as the outer domain is never reached by the liquid. The vertical lines indicate the start and end of the experimental entrapment regime. (d) Spreading behavior for $\theta_1 > \theta_2$ and constant $We = 95$. Droplets impact on disks of varying diameters, where $\theta_1 = 157°$ and $\theta_2 = 124°$. As D_{Area} rises, the maximum spreading diameter declines until the inner region is large enough for the entire spreading to occur within it. The vertical line divides the graph into exterior (to the left) and interior (to the right) spreading regimes.

the exterior region, the contact angle would have to transition from a higher energy state to a lower energy state, which is energetically favorable, and thus this would occur spontaneously. The ΔE_{bar} term for such cases would be nonexistent. In essence, there would be only two regimes of spreading, namely interior and exterior spreading. For interior spreading, the maximum spreading diameter can be calculated from

$$(We + 12)\eta_l = 8 + \eta_l^3\left[3(1 - \cos\theta_1) + \frac{4We}{\sqrt{Re}}\right]. \quad (10)$$

On the other hand, the maximum spreading diameter in the exterior spreading regime can be calculated from Equation (6) without the ΔE_{bar}, with all other terms as previously defined, that is,

$$E_{S1} + E_{K1} = E_{S2} - \sigma\frac{\pi}{4}D_{Area}^2\cos\theta_1$$
$$- \sigma\frac{\pi}{4}\left(D_{Max}^2 - D_{Area}^2\right)\cos\theta_2 + W_{losses}. \quad (11)$$

It is noted that Equation (11) includes terms dependent on both θ_1 and θ_2. Thus, in the case where $\theta_2 < \theta_1$, the wettability of the inner region influences spreading in the exterior region. In contrast, Equation (7) for $\theta_2 > \theta_1$ had no dependence on θ_1. We verified this experimentally by observing water droplets impacting nonwettable circular domains surrounded by more wettable surfaces. We see from Figure 4d, in the case of constant $We = 95$ and varying target disk sizes, the wettability of the inner region does affect the maximum spreading diameter in the exterior spreading regime. As the diameter

WILEY-**Droplet**

of the inner region ($\theta_1 = 157°$) increases, the maximum exterior spreading diameter declines. This effect can also be theoretically verified through Equation (11), which includes a θ_1 term in the calculation of the maximum spreading diameter. Plugging in the values, the theoretical predictions also follow the same trend as observed in the experiments (see Figure 4d). Intuitively, in the interior spreading regime, the maximum spreading diameter for a given *We* remains insensitive to D_{Area}, as seen, for $D_{Area} > 6$ mm in Figure 4d.

CONCLUSION

We studied experimentally and analytically three distinct regimes of dynamic axisymmetric spreading when water droplets (with Weber number less than 60) impact centrally on a circular target (disk) surrounded by an area of different wettability. The spreading regimes arise from the existence of a cross-over energy barrier that the spreading liquid must overcome when crossing suddenly onto a surface of lower wettability (higher contact angle). We interpreted the observations with a simple analytical formulation based on the energy balance of the impacting droplet. The corresponding analysis showed how under such circumstances, the spreading in the outer region was not influenced by the wettability of the inner region. The scaling of the theoretical equations and the predictions of the maximum spreading diameter were consistent with the experimental observations and further corroborated the existence of different regimes of axisymmetric droplet spreading on nonuniform wettability surfaces. Experiments were also performed for dual-domain situations where the outer region was more wettable than the inner one. Overall, the theoretical understanding put forth here explains and agrees with the experimental results produced in this configuration. The model—albeit simple—is capable of predicting the salient features of the wetting dynamics of the droplet impact experiments. Follow-up numerical studies are needed to accurately predict the spreading dynamics while taking into consideration the viscous and kinetic losses in configurations where the target surface features spatially complex wettability. The present study may assist the design of engineered surfaces with wettability modifications intended to induce desired droplet impact outcomes.

METHODS

The surfaces used in the experiments were fabricated via a facile and scalable fabrication method to create the nonuniform wettability-patterned surfaces. Aluminum (Al) plates (mirror finished Al; 6061, McMaster-Carr) of dimensions 25 mm × 25 mm were cleaned, rinsed with ethanol (200 proof; Decon Labs), and DI water, and dried. To make certain areas of the Al surface superhydrophobic, a Yb laser (100% power, 10 kHz pulse frequency, 200 mm/s rastering speed EMS300; Tykma Electrox) was used to selectively etch away some metal to impart roughness to the surface. The samples were then spin-coated with Teflon AF (Chemours AF 2400; 1%) at 2000 rpm for

20 s using a WS-400-6NPP-LITE Spin Coater. After the Teflon was applied, the samples were cured on a laboratory hot plate at 80°C for 15 min, then at 180°C for 15 min, and finally at 260°C for 7 min.[61] The Teflon was coated uniformly on both the smooth mirror-finished and the laser-treated parts of the Al sample (see Figure 1a1,a2). When the laser-etched part was a disk of diameter D_{Area} in the center, the resulting pattern was a nonwettable disk surrounded by a relatively more wettable domain. When the laser-etching was done on the entire plate except for a disk of diameter D_{Area} in the center, the resulting sample had a relatively more wettable disk area surrounded by a nonwettable domain (see Figure 1a3). The scanning electron micrographs (SEM) of both domains, that is, Teflon-coated smooth Al and Teflon-coated laser-processed Al are shown in Figure 5b1,b2. The SEM images revealed no characteristic micro-nanostructures on the Teflon-coated smooth Al, contrary to those observed on the Teflon-coated laser-textured substrate. This resulted in the difference in wettabilities (see Figure 5).

To characterize the wettability of each domain, we measured the static and dynamic contact angles of DI water using an in-house goniometer following the method of Moitra et al.[18] (see Figure 5a1,a2). Two separate uniform-wettability samples were prepared using the same technique as used on the actual test samples to make the hydrophobic and superhydrophobic regions. These separate uniform-wettability hydrophobic and superhydrophobic samples were then used for contact angle characterization. The super-hydrophobic surface exhibited a static contact angle of 156.7 ± 0.8° and an advancing contact angle of 157 ± 2.9°. The smooth hydrophobic surface exhibited a static contact angle of 115.53 ± 1.03°, and an advancing contact angle of 124.48 ± 3.1°. The dynamic contact angles reported in this work were measured as follows. A liquid volume of DI water with a diameter of 2.1 mm was deposited through a syringe on a uniform-wettability surface and allowed to come to equilibrium (still attached to the syringe needle). Subsequently, the volume of this droplet was increased at a steady rate of 1.5 μL/s so that the contact line advanced steadily.[62,63] The angle formed by the liquid front in this configuration defines the advancing contact angle and was used throughout to characterize the wettability of the different surface domains in this work. The aforementioned contact angles were deduced by averaging the contact angle of both advancing sides (left and right) for three separate (six readings) substrates prepared in the same manner for each wettability.

In the analytical portion of this work, we substituted the advancing angle into equations that are generally used in conjunction with the static/equilibrium contact angle. There is an ongoing discussion on the validity of this substitution. Authors like Pasandideh-Fard et al.,[55] or Ukiwe and Kwok[57] have noted this type of substitution to be valid and have used the advancing contact angle in their analytical calculations. Relying on the present experimental measurements, we maintain that the use of the advancing angle is physically valid and consistent for the situations examined herein. The density, surface tension, and viscosity of DI water were measured at room temperature of 25°C and found to be 998 kg/m³, 72 mN/m, and $0.93 × 10^{-3}$ Pa s, respectively.
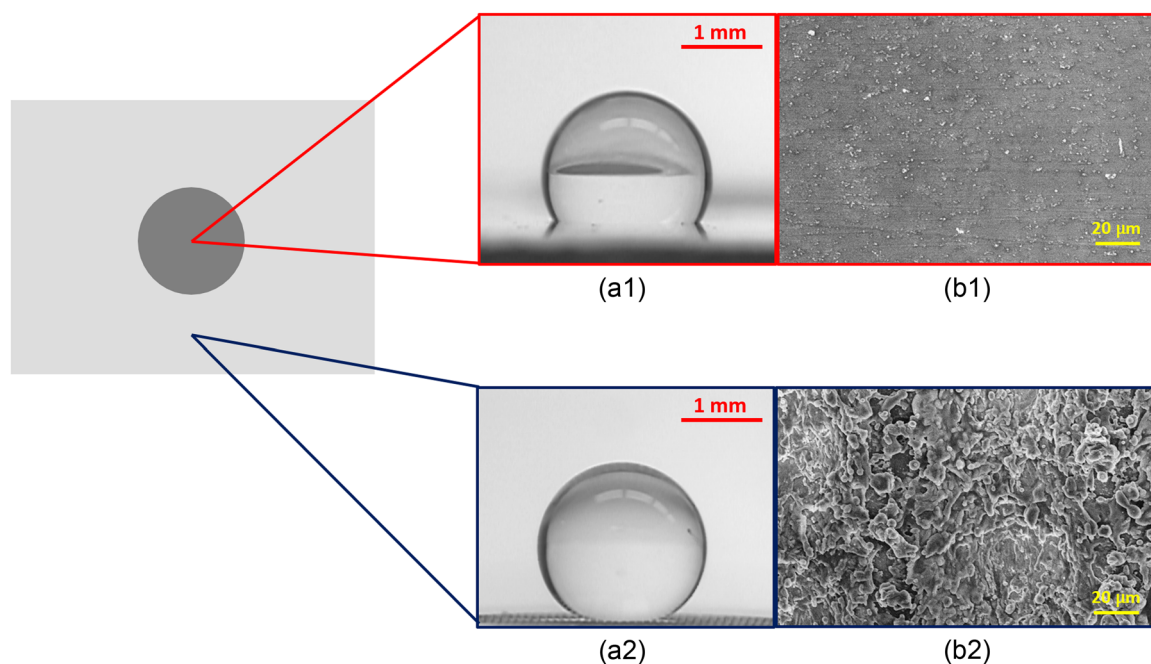
FIGURE 5 Characterization of the two distinct spatial domains of wettability. (a1) Sessile water droplet on Teflon-coated smooth aluminum (static θ_{s1} = 115°). (b1) Scanning electron microscope (SEM) image of the Teflon-coated smooth aluminum. (a2) Sessile water droplet on Teflon-coated laser-processed aluminum (static θ_{s2} = 157°). (b2) SEM micrograph of the Teflon-coated laser-processed aluminum.

To ensure that the droplets accurately impacted at the center of the circular region, a dual camera setup was utilized (Figure 1b). The setup consisted of a floating optical table, illuminated by a cold light source (Rosco LitePad Axiom), a high-speed camera (Vision Phantom M310), and a DSLR camera (Nikon J1 with Nikkor 30–110 mm zoom lens) used in a synchronized fashion to capture each impact event; see Figure 1b. The DSLR camera was used to capture images from the side only to ensure that the droplet impacted orthogonally and centrally on the substrate as viewed from both directions. The maximum spreading of the droplets during each impact was recorded using the high-speed camera at 800 frames per second with 1200 μs exposure time. The images from the high-speed camera were analyzed using the ImageJ software, the Phantom Camera software, and an in-house MATLAB script to determine the maximum spreading of the droplets in each case. The setup was covered with a clear transparent acrylic box so as to avert disturbances to the droplet impact direction and velocity.

CONFLICT OF INTEREST STATEMENT
The authors declare no conflicts of interest.

ORCID
Shashwata Moitra http://orcid.org/0000-0002-1954-330X
Constantine M. Megaridis http://orcid.org/0000-0002-6339-6933

REFERENCES
1. Worthington AM. On the forms assumed by drops of liquids falling vertically on a horizontal plate. *Proc R Soc London*. 1876; 25:261-272.
2. Yarin AL. Drop impact dynamics: splashing, spreading, receding, bouncing.... *Annu Rev Fluid Mech*. 2006;38:159-192.
3. Josserand C, Thoroddsen ST. Drop impact on a solid surface. *Annu Rev Fluid Mech*. 2016;48:365-391.
4. Chandra S, Avedisian CT. On the collision of a droplet with a solid surface. *Proc R Soc London Ser A*. 1991;432:13-41.
5. Khojasteh D, Kazerooni M, Salarian S, Kamali R. Droplet impact on superhydrophobic surfaces: a review of recent developments. *J Ind Eng Chem*. 2016;42:1-14.
6. Bartolo D, Bouamrirene F, Verneuil É, Buguin A, Silberzan P, Moulinet S. Bouncing or sticky droplets: impalement transitions on superhydrophobic micropatterned surfaces. *Europhys Lett*. 2006;74: 299.
7. Bayer IS, Megaridis CM. Contact angle dynamics in droplets impacting on flat surfaces with different wetting characteristics. *J Fluid Mech*. 2006;558:415-449.
8. Du J, Wang X, Li Y, Min Q, Wu X. Analytical consideration for the maximum spreading factor of liquid droplet impact on a smooth solid surface. *Langmuir*. 2021;37:7582-7590.
9. Fukai J, Zhao Z, Poulikakos D, Megaridis CM, Miyatake O. Modeling of the deformation of a liquid droplet impinging upon a flat surface. *Phys Fluids A*. 1993;5:2588-2599.
10. Fukai J, Shiiba Y, Yamamoto T, et al. Wetting effects on the spreading of a liquid droplet colliding with a flat surface: experiment and modeling. *Phys Fluids*. 1995;7:236-247.
11. Reyssat M, Pardo F, Quéré D. Drops onto gradients of texture. *Europhys Lett*. 2009;87:36003.
12. Richard D, Quéré D. Bouncing water drops. *EPL*. 2000;50:769.
13. Schutzius TM, Jung S, Maitra T, Graeber G, Köhme M, Poulikakos D. Spontaneous droplet trampolining on rigid superhydrophobic surfaces. *Nature*. 2015;527:82-85.

14. Megaridis CM, Boomsma K, Bayer IS. Partial rebound of molten-metal droplets impacting on solid substrates. *AIChE J.* 2004;50: 1356-1363.

15. Liu Y, Moevius L, Xu X, Qian T, Yeomans JM, Wang Z. Pancake bouncing on superhydrophobic surfaces. *Nat Phys.* 2014;10: 515-519.

16. Bird JC, Dhiman R, Kwon HM, Varanasi KK. Reducing the contact time of a bouncing drop. *Nature.* 2013;503:385-388.

17. Jafari Gukeh M, Moitra S, Ibrahim AN, Derrible S, Megaridis CM. Machine learning prediction of TiO_2-coating wettability tuned via UV exposure. *ACS Appl Mater Interfaces.* 2021;13: 46171-46179.

18. Moitra S, Roy T, Ganguly R, Megaridis CM. Jet impact on superhydrophobic metal mesh. *Langmuir.* 2021;37:2891-2899.

19. Gukeh MJ, Damoulakis G, Megaridis CM. Low-profile heat pipe consisting of wick-lined and non-adiabatic wickless wettability-patterned surfaces. *Appl Therm Eng.* 2022;211:118433.

20. Koukoravas TP, Damoulakis G, Megaridis CM. Experimental investigation of a vapor chamber featuring wettability-patterned surfaces. *Appl Therm Eng.* 2020;178:115522.

21. Ghosh A, Beaini S, Zhang BJ, Ganguly R, Megaridis CM. Enhancing dropwise condensation through bioinspired wettability patterning. *Langmuir.* 2014;30:13103-13115.

22. Chang W, Luo K, Wang P, Abdulshaheed AA, Li C. Sustainable dropwise condensation enabled ultraefficient heat pipes. *Droplet.* 2023;2:e43.

23. Xu W, Zheng H, Liu Y, et al. A droplet-based electricity generator with high instantaneous power density. *Nature.* 2020;578:392-396.

24. Jiang M, Wang Y, Liu F, et al. Inhibiting the Leidenfrost effect above 1,000 C for sustained thermal cooling. *Nature.* 2022;601: 568-572.

25. Ghosh A, Ganguly R, Schutzius TM, Megaridis CM. Wettability patterning for high-rate, pumpless fluid transport on open, non-planar microfluidic platforms. *Lab Chip.* 2014;14:1538-1550.

26. Liang X, Kumar V, Ahmadi F, Zhu Y. Manipulation of droplets and bubbles for thermal applications. *Droplet.* 2022;1:80-91.

27. Xu J, Xiu S, Lian Z, Yu H, Cao J. Bioinspired materials for droplet manipulation: principles, methods and applications. *Droplet.* 2022; 1:11-37.

28. Bai H, Wang L, Ju J, Sun R, Zheng Y, Jiang L. Efficient water collection on integrative bioinspired surfaces with star-shaped wettability patterns. *Adv Mater.* 2014;26:5025-5030.

29. Yu Z, Yun FF, Wang Y, et al. Desert beetle-inspired superwettable patterned surfaces for water harvesting. *Small.* 2017;13:1701403.

30. Wang Y, Zhang L, Wu J, Hedhili MN, Wang P. A facile strategy for the fabrication of a bioinspired hydrophilic-superhydrophobic patterned surface for highly efficient fog-harvesting. *J Mater Chem A.* 2015;3:18963-18969.

31. Elsharkawy M, Schutzius TM, Megaridis CM. Inkjet patterned superhydrophobic paper for open-air surface microfluidic devices. *Lab Chip.* 2014;14:1168-1175.

32. Koukoravas TP, Ghosh A, Mahapatra PS, Ganguly R, Megaridis CM. Spatially-selective cooling by liquid jet impinging orthogonally on a wettability-patterned surface. *Int J Heat Mass Transfer.* 2016;95: 142-152.

33. Yang X, Liu X, Lu Y, et al. Controllable water adhesion and anisotropic sliding on patterned superhydrophobic surface for droplet manipulation. *J Phys Chem C.* 2016;120:7233-7240.

34. Xu C, Feng R, Song F, et al. Continuous and controlled directional water transportation on a hydrophobic/superhydrophobic patterned surface. *Chem Eng J.* 2018;352:722-729.

35. Qi W, Weisensee PB. Dynamic wetting and heat transfer during droplet impact on bi-phobic wettability-patterned surfaces. *Phys Fluids.* 2020;32:067110.

36. Zupančič M, Steinbücher M, Gregorčič P, Golobič I. Enhanced pool-boiling heat transfer on laser-made hydrophobic/superhydrophilic polydimethylsiloxane-silica patterned surfaces. *Appl Therm Eng.* 2015;91:288-297.

37. Thomas OC, Cavicchi RE, Tarlov MJ. Effect of surface wettability on fast transient microboiling behavior. *Langmuir.* 2003;19: 6168-6177.

38. Wang X, Wang Y-B, Gao S-R, Yang Y-R, Wang X-D, Lee D-J. Controllable splitting of impacting droplets by hybrid-wettability surface. *J Taiwan Inst Chem Eng.* 2020;111:24-33.

39. Yuan Z, Matsumoto M, Kurose R. Directional migration of an impinging droplet on a surface with wettability difference. *Phys Rev Fluids.* 2020;5:113605.

40. Huang J, Wang L, He K. Three-dimensional study of double droplets impact on a wettability-patterned surface. *Comput Fluids.* 2022;248:105669.

41. Ji T, Pan Y, Shao Y, He B, Wen B. Lateral drop rebound on a hydrophobic and chemically heterogeneous surface. *Langmuir.* 2021;37:6905-6914.

42. Vaikuntanathan V, Kannan R, Sivakumar D. Impact of water drops onto the junction of a hydrophobic texture and a hydrophilic smooth surface. *Colloids Surf A.* 2010;369:65-74.

43. Vaikuntanathan V, Sivakumar D. Directional motion of impacting drops on dual-textured surfaces. *Phys Rev E.* 2012;86:036315.

44. Kim S, Moon MW, Kim HY. Drop impact on super-wettability-contrast annular patterns. *J Fluid Mech.* 2013;730:328-342.

45. Mock U, Michel T, Tropea C, Roisman I, Rühe J. Drop impact on chemically structured arrays. *J Phys Condens Matter.* 2005;17: S595-S605.

46. Michel T, Mock U, Roisman IV, Rühe J, Tropea C. The hydrodynamics of drop impact onto chemically structured surfaces. *J Phys Condens Matter.* 2005;17:S607-S622.

47. Schutzius TM, Graeber G, Elsharkawy M, Oreluk J, Megaridis CM. Morphing and vectoring impacting droplets by means of wettability-engineered surfaces. *Sci Rep.* 2014;4:7029.

48. Zhang T, Wu J, Lin X. Lateral motion of a droplet impacting on a wettability-patterned surface: numerical and theoretical studies. *Soft Matter.* 2021;17:724-737.

49. Sprittles J, Shikhmurzaev Y. The dynamics of liquid drops and their interaction with solids of varying wettabilities. *Phys Fluids.* 2012; 24:082001.

50. Russo A, Icardi M, Elsharkawy M, Ceglia D, Asinari P, Megaridis CM. Numerical simulation of droplet impact on wettability-patterned surfaces. *Phys Rev Fluids.* 2020;5:074002.

51. Farshchian B, Pierce J, Beheshti MS, Park S, Kim N. Droplet impinging behavior on surfaces with wettability contrasts. *Microelectron Eng.* 2018;195:50-56.

52. Xu J, Chen Y, Xie J. Non-dimensional numerical study of droplet impacting on heterogeneous hydrophilicity/hydrophobicity surface. *Int J Heat Mass Transfer.* 2018;116:951-968.

53. Sen U, Roy T, Chatterjee S, Ganguly R, Megaridis CM. Post-impact behavior of a droplet impacting on a permeable metal mesh with a sharp wettability step. *Langmuir.* 2019;35:12711-12721.

54. Satpathi NS, Malik L, Ramasamy AS, Sen AK. Drop impact on a superhydrophilic spot surrounded by a superhydrophobic surface. *Langmuir.* 2021;37:14195-14204.

55. Pasandideh-Fard M, Qiao Y, Chandra S, Mostaghimi J. Capillary effects during droplet impact on a solid surface. *Phys Fluids.* 1996;8: 650-659.

56. Mao T, Kuhn D, Tran H. Spread and rebound of liquid droplets upon impact on flat surfaces. *AIChE J.* 1997;43:2169-2179.

57. Ukiwe C, Kwok DY. On the maximum spreading diameter of impacting droplets on well-prepared solid surfaces. *Langmuir.* 2005; 21:666-673.

58. Healy WM, Hartley JG, Abdel-Khalik S. Surface wetting effects on the spreading of liquid droplets impacting a solid surface at low Weber numbers. *Int J Heat Mass Transfer*. 2001;44: 235-240.

59. Roisman IV, Rioboo R, Tropea C. Normal impact of a liquid drop on a dry surface: model for spreading and receding. *Proc R Soc London Ser A*. 2002;458:1411-1430.

60. Madejski J. Solidification of droplets on a cold surface. *Int J Heat Mass Transfer*. 1976;19:1009-1013.

61. Jafari Gukeh M, Roy T, Sen U, Ganguly R, Megaridis CM. Lateral spreading of gas bubbles on submerged wettability-confined tracks. *Langmuir*. 2020;36:11829-11835.

62. Sarkar S, Roy T, Roy A, Moitra S, Ganguly R, Megaridis CM. Revisiting the supplementary relationship of dynamic contact angles measured by sessile-droplet and captive-bubble methods: role of surface roughness. *J Colloid Interface Sci*. 2021;581:690-697.

63. Sarkar S, Jafari Gukeh M, Roy T, et al. A new methodology for measuring solid/liquid interfacial energy. *J Colloid Interf Sci*. 2023;633:800-807.

SUPPORTING INFORMATION

Additional supporting information can be found online in the Supporting Information section at the end of this article.